



# Simple and scalable fabrication of hairy ZnO@ZnS core@shell Cu cables for continuous sunlight-driven photocatalytic water remediation

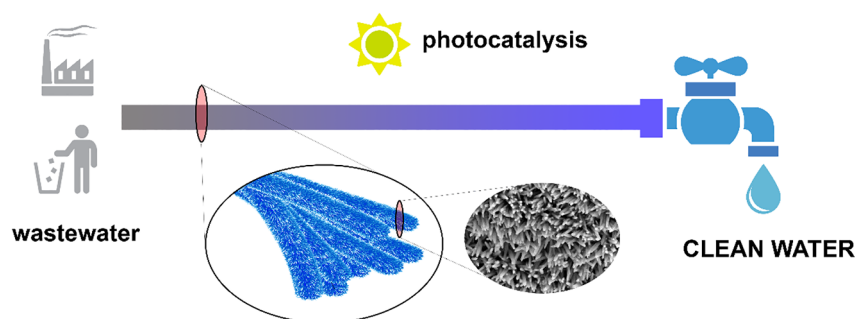
Albert Serrà\*, Laetitia Philippe

Empa, Swiss Federal Laboratories for Materials Science and Technology, Laboratory for Mechanics of Materials and Nanostructures, Feuerwerkerstrasse 39, CH-3602 Thun, Switzerland

## HIGHLIGHTS

- Scalable and holistic strategy for synthesizing hairy ZnO-based photocatalysts is proposed.
- Integration of ZnO-based immobilized photocatalysts in continuous flow tubular-type reactor.
- Excellent UV-filtered continuous mineralization of persistent organic pollutants.
- ZnO@ZnS heterostructure improved UV-filtered light absorption and photocorrosion-resistance.
- Recyclability of photocatalysts and system are also discussed.

## GRAPHICAL ABSTRACT



## ARTICLE INFO

### Keywords:

Photocatalysis  
ZnO-based photocatalysts  
Sunlight  
Reactor design  
Photocatalyst synthesis

## ABSTRACT

Over the last few decades, the application of photocatalysis for mineralizing persistent organic pollutants and other new emerging contaminants has gained increasing research and industry attention. However, the integration of catalyst fabrication and reactor design has not yet been realized for photocatalytic water decontamination applications. Herein, we present, for the first time, a facile, scalable, and eco-friendly strategy for the direct synthesis and integration of hairy ZnO@ZnS core@shell Cu cables in a continuous flow tubular-type reactor. The hairy ZnO@ZnS core@shell Cu cables exhibited (i) excellent photocatalytic performance (photocatalytic degradation > 99%, mineralization > 99%) for continuous water decontamination of both single-(methylene blue) and multi-pollutants (methylene blue, p-nitrophenol, and rhodamine B) under artificial UV-filtered sunlight irradiation; (ii) a large surface area ( $90.1 \text{ m}^2 \text{ g}^{-1}$ ) and a large number of active sites owing to the hairy architecture; (iii) enhanced light absorption in the visible region due to the ZnO@ZnS core@shell heterostructure, which promotes the separation of photogenerated carriers; (iv) improved light trapping capability due to the hairy architecture; (v) high photostability with minimal photocorrosion (< 2% after 180 h of continuous irradiation); and (vi) excellent robustness. The recyclability and potential for direct re-fabrication of a fresh photocatalyst were also successfully confirmed. Thus, hairy ZnO@ZnS core@shell Cu cables were demonstrated to be a reliable and promising immobilized photocatalysts for the efficient mineralization of persistent organic pollutants and for the total/partial oxidation of other emerging pollutants in a continuous flow tubular-type reactor.

\* Corresponding author.

E-mail address: [albert.serramos@empa.ch](mailto:albert.serramos@empa.ch) (A. Serrà).

<https://doi.org/10.1016/j.cej.2020.126164>

Received 21 April 2020; Received in revised form 28 June 2020; Accepted 30 June 2020

Available online 05 July 2020

1385-8947/ © 2020 The Author(s). Published by Elsevier B.V. This is an open access article under the CC BY license (<http://creativecommons.org/licenses/by/4.0/>).

## 1. Introduction

According to the United Nations world water development report 2018, more than five billion people (mostly in developing countries) could suffer water shortages by 2050 due to climate change, increased demand, rampant human activities, and polluted supplies. The treatment and potential reuse of contaminated water is a vital factor for mitigating this problem throughout the world [1,2]. Conventional wastewater treatment systems involving various physical, chemical, and biological processes are effective for destroying commonly found organic and inorganic pollutants [3–5]. However, many persistent organic pollutants (e.g. pesticides, herbicides, dyes, surfactants) and/or new emerging contaminants (e.g. trace organic compounds, nanoparticles, microplastics, cyanotoxins, or antibiotics) are present in water in increasing concentrations and are not affected by conventional treatment processes. Because of persistent and emerging contaminants, which pose potential threats to the environment and which can damage human health through various exposed pathways (e.g. direct ingestion, dermal contact), development of new technologies and revision of conventional water treatment processes are necessitated [6–9].

Considerable research has been focused on advanced oxidation processes (AOPs) because of their potential to enable the removal of persistent and emerging pollutants [5–9]. Photocatalysis offers significant advantages over other AOPs because of its favorable operation conditions, including the capability to use solar light as a radiation source, thus reducing energy costs and consumption. Photocatalytic technologies are, thus, an environmentally friendly and sustainable alternative to conventional water treatment processes, allowing for the integration of green and circular chemistry principles, namely, reducing waste production while utilizing energy, water, and other resources more efficiently [8,10–13]. Photocatalysis has been conducted for the efficient removal of various organic compounds, including persistent organic pollutants, as well as for the inactivation of different types of pathogens such as viruses, cyanobacteria, and fungi at the laboratory scale. However, it is seldom used in industrial or domestic applications. Thus, the integration of photocatalysis as a pre- or post-treatment process in conventional wastewater treatment process could revolutionize the water technology industry [14,15].

Over the past 30 years, catalyst fabrication methods and their effects on the photocatalytic performance and catalyst stability (photo- and chemical stability) as well as the mechanisms responsible for mineralization (i.e., conversion of organic pollutants into intermediate compounds and subsequently into carbon dioxide and water) have been widely investigated [14–17]. Moreover, a few studies have focused on the efficient integration and/or immobilization of photocatalysts in photocatalytic systems (e.g., wall, fixed-bed reactors) to allow for continuous wastewater treatment while avoiding the need for post-treatment processes for photocatalyst separation and recuperation [13,18–21]. However, the integration of catalyst fabrication and reactor design has not been extensively investigated, thus inhibiting the industrial/domestic applicability of photocatalytic water decontamination. The efficient design of photocatalytic reactors is likely to be a key factor for process development, and consequently, will become a future interdisciplinary challenge to both scientists and engineers.

Over the last few decades, different types of catalytic reactors have been proposed to maximize productivity in various applications, improve selectivity, and solve safety issues. In the field of reactor design, the concepts of reactivity, kinetics, robustness, transport phenomena, and reactor modelling are intimately integrated in a complex process for full-fledged industrial reactor optimization [22–24]. However, the design of photocatalytic reactors for water decontamination extends the complexity of catalytic reactor scale-up due to the need to utilize a solid photocatalyst (i.e. multiphase photocatalytic reactor) and the requirement for additional engineering factors related to photocatalyst illumination (i.e. the distribution of light, light propagation, light scattering, depth of radiation penetration, and local volumetric light

absorption). Among the multiple challenges affecting photoreactor design, the reduction of photocorrosion and the chemical and mechanical leaching rate, which cause a gradual loss of the photocatalytic performance, are possibly the major concerns as they affect photoreactor scalability. Over the last two decades, tremendous efforts have been devoted for the improvement of the chemical, photochemical, and mechanical stability of immobilized photocatalysts. Importantly, the applicability of direct solar irradiation has increased the amount of interest in photocatalysis, but introduces an additional degree of complexity due to the requirement for a transparent surface, which can dramatically affect the reactor design [25–27]. However, the improvement of light transport technology, along with the development of low-loss optical fibers and the revolution in LED technology, has stimulated interest in applying photocatalysis to water decontamination [28,29].

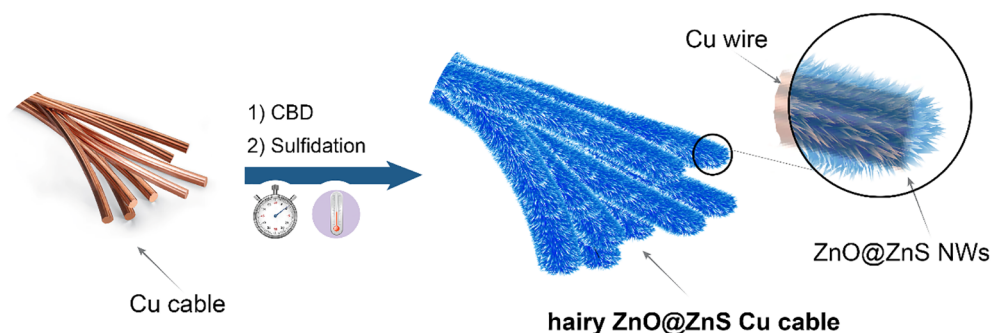
Herein, we propose a novel, simple, inexpensive, green, and scalable strategy for the direct synthesis and integration of efficient visible-light hairy ZnO@ZnS core@shell Cu cables in silicone tubes for continuous wastewater treatment, thus realizing the integration of catalyst fabrication and reactor design. Although various processes have been reported for the synthesis of hairy ZnO nanostructures, none of those studies considered the direct synthesis and integration of immobilized photocatalysts for developing tubular continuous flow photoreactors [30–39]. This study demonstrates that hairy ZnO@ZnS core@shell Cu cables can be integrated and scaled-up in different reactor systems, because of the simplicity of the synthesis process. Excellent photocatalytic performance and reusability were demonstrated for the removal of different persistent organic pollutants (a single-pollutant solution of methylene blue (MB) and a multi-pollutant solution of MB + 4-nitrophenol (4-NP) + Rhodamine B (Rh B)) under UV-filtered artificial sunlight using a recirculating reactor system. Additionally, the photostability, photocatalyst leaching rate, and photocorrosion resistance of the hairy ZnO@ZnS core@shell Cu cables were determined under continuous UV-filtered irradiation. The excellent robustness of immobilized photocatalysts is pivotal for scalability. A good photocatalyst design, especially for environmentally friendly applications, must integrate the principles of green and circular chemistry and address the issues of recyclability or integration in a circular process to minimize the generation of residues. Thus, the recyclability potential of the proposed system was demonstrated using fresh hairy ZnO@ZnS core@shell Cu cables that could be resynthesized using the same recycled substrate while allowing for the recuperation of Zn and Cu ions.

## 2. Experimental

### 2.1. Synthesis and characterization of hairy ZnO@ZnS core@shell Cu cables

The direct growth of hairy ZnO@ZnS core@shell Cu cables inside a silicone tube (Fig. S1) offered a scalable and economically feasible synthetic procedure for fabricating potential tube reactors for water purification using sunlight irradiation. Optimization of the design and standardization of the reactor components have not been addressed in the present work. Note that similar, though more complex, systems have already been tested in a pilot-plant scale. The synthesis was a multi-step process based on:

- (i) *Photocatalyst substrate preparation.* The polyvinyl chloride insulation layer of a 6 mm diameter Cu cable composed of 40 0.3 mm diameter Cu wires was removed (Fig. S1a). The Cu cable was then inserted and fixed through a 10 mm diameter silicone tube (Fig. S1b), which was then connected to a water pump circuit (Fig. S1c). The silicone tubes and Cu cable were then rinsed in an ethanol-water (1:3) solution for 30 min.
- (ii) *Zinc oxide chemical deposition.* To deposit ZnO nanowires on the Cu wires, a constant flow ( $0.2 \text{ L min}^{-1}$ ) of an oxygen-saturated



**Scheme 1.** Schematic representation of the synthesis of hairy ZnO@ZnS core@shell Cu cables. CBD: chemical bath deposition. Note that Cu cables were integrated inside the silicone tube prior to the start of the synthesis in order to meet the photocatalyst fabrication and reactor design. The synthesized hairy ZnO@ZnS core@shell Cu cables were kept inside the transparent silicone tube for the whole process mimicking a tubular reactor.

solution of 5 mM zinc (II) nitrate (Sigma-Aldrich, > 99%) and a 3 mM borane dimethylamine complex (DMAB; Sigma-Aldrich, 97%) was circulated through the tube for a set period of time, resulting in the formation of a hairy ZnO Cu cable (Scheme 1). The temperature of the deposition bath was maintained at 80 °C. The silicone tubes and hairy ZnO Cu cables were rinsed in an ethanol:water (1:3) solution for 30 min.

- (iii) **Sulfidation.** To form a thin shell of ZnS on a hairy ZnO Cu cable, a constant flow (0.2 L min<sup>-1</sup>) of a 30 mM thioacetamide (Sigma-Aldrich, 98%) solution was circulated through the silicone tube for 3 h at 85 °C (Scheme 1), resulting in hairy ZnO@ZnS Cu cables.

The morphology of the hairy ZnO@ZnS Cu cables was examined by field-emission scanning electron microscopy (5 kV, FE-SEM; Hitachi S-4800) with energy-dispersive X-ray spectroscopy. Specific surface areas were measured in accordance with the Brunauer-Emmett-Teller (BET) method from nitrogen adsorption-desorption isotherms obtained at 77 K using a Micrometrics Tristar-II. The crystal phases were determined by X-ray diffraction patterns measured with a Bruker D8 Discovery diffractometer. A 2θ scan between 20° and 80° was used, with a step size of 0.05 and a measuring time of 15 s per step. X-ray photoelectron spectroscopy (XPS) measurements were taken with an XPS system (PHI 5600 Multitechnique, Physical Electronics) using a monochromatic X-ray source (Al K<sub>α</sub> line = 1486.6 eV, 350 W). The area analyzed was a circle 0.6 mm in diameter, and all measurements were made in an ultra-high vacuum chamber. ZnO and ZnO@ZnS Cu cables were etched by means of argon ion sputtering up to a few nanometers prior to acquiring angle-resolved (AR) XPS images. For FE-SEM, BET, XRD, and XPS analysis, the samples were cut into small pieces prior to being characterized. The optoelectronic properties were examined by collecting diffuse reflectance spectra in the wavelength range of 250 to 800 nm using a Perkin Lambda 900 UV spectrophotometer, whereas the photoluminescence spectra were examined at room temperature by using a PerkinElmer LS-55 fluorescence spectrometer.

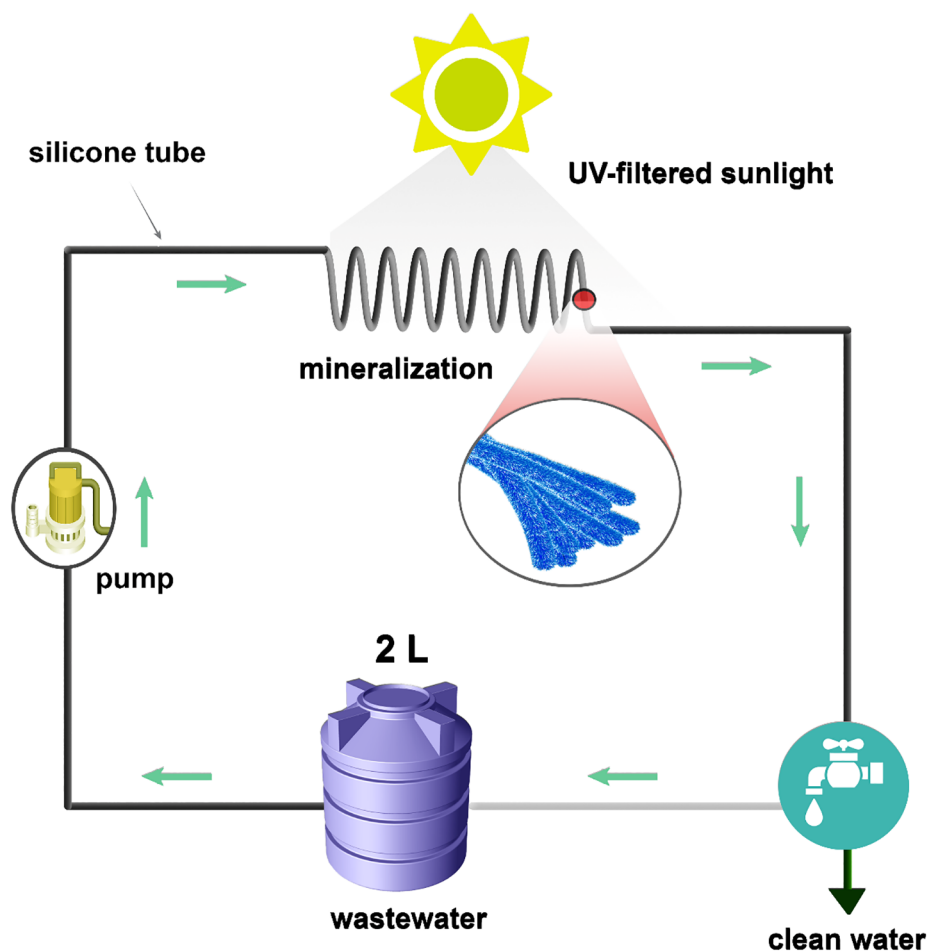
## 2.2. Photocatalytic activity of hairy ZnO@ZnS core@shell Cu cables

The photocatalytic activity of ZnO and ZnO@ZnS core@shell Cu cables was evaluated by degradation of a 10 ppm methylene blue (MB) solution under artificial UV-filtered sunlight irradiation using our photoreactor (Scheme 2). Artificial UV-filtered sunlight ( $\lambda > 400$  nm, light intensity of  $450 \pm 20$  lx, irradiance of  $8 \times 10^{-3}$  W cm<sup>-2</sup>) was generated using 500 W Xe lamp irradiation with a 400 nm cut-off filter. The temperature, photocatalyst dosage, volume of polluted solutions, and flux rate were fixed and maintained at 25 °C, 0.7 g, 2 L, and 0.25 L min<sup>-1</sup>, respectively. The pH of the solution was adjusted to 7.0 for all the experiments. Prior to irradiation, polluted solutions were circulated in dark conditions for 1 h to reach adsorption-desorption equilibrium. At set time intervals during UV-filtered irradiation, 2.5 mL aliquots were collected for analysis. The concentration of MB was determined by UV-vis spectroscopy at its maximum absorption wavelength ( $\lambda = 662$  nm) using a UV-vis PerkinElmer Lambda 900 UV

spectrophotometer. Photocatalytic mineralization (i.e. degradation of MB into intermediate compounds and subsequently into CO<sub>2</sub> and H<sub>2</sub>O) was also examined by comparing the total organic content (TOC) prior to the start of irradiation and after circulating the pollutant solution for 65 min using a TOC analyzer (model TOC-V<sub>CSH</sub>). Each experiment was repeated four times to ensure accuracy and reproducibility. To evaluate the effect of flux rate on the mineralization of MB, the reduction of the TOC content after 45 min of irradiation of a 10-ppm MB solution was determined at different flow rate, ranging from 0.05 to 1.5 L min<sup>-1</sup>. To investigate the role of the reactive species involved in the photocatalytic process (i.e., hydroxyl radicals, oxygen superoxide, and photogenerated holes), the quenching of chemical selective radicals was performed. For an indicator, a pollutant solution of 10-ppm MB was used that contained (a) isopropyl alcohol (Sigma-Aldrich, > 99.7%), a quencher of hydroxyl radicals, (b) benzoquinone (Sigma-Aldrich, > 98%), a quencher of superoxide radicals, or (c) triethanolamine (Sigma-Aldrich, > 99%), a quencher for photogenerated hole, which were independently added until a concentration of 1 mM was obtained. The maximum absorption peak intensity of MB 662 nm after 45 min of UV-filtered sunlight irradiation was recorded. Additionally, to confirm the catalytic performance of ZnO@ZnS core@shell Cu cables for the mineralization of persistent organic pollutants, a mixture of MB (25 ppm) + 4-NP (25 ppm) + Rh-B (25 ppm) was circulated for 6 h under UV-filtered irradiation. The photocatalytic mineralization of this mixture was followed by observing the color changes in the solution throughout circulation and measuring the TOC after 6 h of circulation.

## 2.3. Photostability of hairy ZnO@ZnS core@shell Cu cables

To evaluate the photocatalyst reusability and robustness, the MB photocatalytic degradation performance was confirmed by repeated photocatalytic experiments (10 times) using the same photocatalyst sample under the same reaction conditions. The photostability of the ZnO@ZnS core@shell Cu cables was also evaluated by measuring the time-dependent concentrations of Zn(II) and Cu(II) ions in the circulating water over a period of 180 h under artificial UV-filtered sunlight irradiation. The concentration of Zn(II) ions was determined spectrophotometrically using Zincon monosodium salt (Sigma-Aldrich) in borate buffer (50 mM, pH = 9) and measuring the absorbance at 620 nm associated with the Zn(II)-bound Zincon complex [40]. The concentration of Cu(II) ions was also spectroscopically determined using 4,4'-bis-(dimethylamino)-thiobenzophenone (TMK; Sigma-Aldrich) in an acetic acid buffer solution (100 mM, pH = 4.6) and a surfactant polyethylene octyl phenyl ether (OP) medium and measuring the absorbance at 500 nm associated with the Cu(II)-TMK-OP complex [41,42]. For these measurements, a UV-1800 Shimadzu UV-vis spectrophotometer (Shimadzu Corporation) with a quartz cuvette with an optical length of 1 cm was used. The morphology of ZnO@ZnS core@shell Cu cables after 120 h of artificial UV-filtered sunlight irradiation was also determined using FE-SEM.



**Scheme 2.** Schematic representation of the proposed photoreactor used in our lab, which incorporated ZnO@ZnS core@shell Cu cables. 2 L of single- or multi-pollutant solutions circulated inside a transparent silicone tube to proceed with the photocatalytic mineralization. The hairy ZnO@ZnS core@shell Cu cables were only integrated into the spiral part of the system, where the artificial UV-filtered sunlight was applied. Note that hairy ZnO@ZnS core@shell Cu cables could be integrated into the whole silicone tube, facilitating the mineralization, but in this preliminary study the photocatalyst was restricted to the spiral area for a better study of the photocatalytic performance.

#### 2.4. Recyclability

After reaching the end of the photocatalyst lifetime (the lifetime of ZnO@ZnS core@shell Cu cables was not determined in this study), Cu cables could be reused to synthesize new ZnO@ZnS core@shell Cu cables. For this purpose, 0.5 M H<sub>2</sub>SO<sub>4</sub> was circulated for 15 min to remove the remaining ZnO@ZnS photocatalyst. MilliQ-Millipore water was then circulated for 5 min for allowing the growth of hairy ZnO@ZnS core@shell nanowires on the Cu wires, facilitating photocatalyst recycling. Zn(II) and Cu(II) were easily recovered and separated by factorial crystallization.

### 3. Results and discussion

#### 3.1. Synthesis and characterization of hairy ZnO@ZnS core@shell Cu cables

The growth of ZnO nanocrystals via a simple palladium-free electroless process was demonstrated on various continuous Cu substrates using DMAB [39]. This strategy opens the door for scalable and non-expensive applications in water decontamination. The experimental conditions (i.e. concentration of precursors, deposition time, and circulating flux) for the Cu-catalyzed growth of hairy ZnO Cu cables in a tubular-type reactor were investigated and optimized. Cu cables were inserted into a silicone tube (Fig. S1), the latter playing a key architectural role in the design of the tubular-type photoreactor. The Cu cables were used to oxidize DMAB and as the seed layer for ZnO growth. The Cu cables, formed by 40 Cu wires,  $300 \pm 25 \mu\text{m}$  in diameter, presented a continuous and uniform surface containing minor defects, scratches, and holes (Fig. S2).

The electroless deposition of ZnO to produce well-defined ZnO nanowires on the Cu wires was then optimized by adjusting the zinc nitrate concentration (i.e., 20, 10, and 5 mM) and circulating flux (i.e., 10 and 2 mL min<sup>-1</sup>). The temperature was maintained at 80 °C for all experiments. The deposition of ZnO crystals strongly depended on the zinc nitrate concentration as the growth density (i.e., number of ZnO grains per unit of area) was inversely proportional to the zinc nitrate concentration. Likewise, as the circulating flux flow rate increased, the growth density decreased significantly. To maximize the ZnO growth density, a zinc nitrate concentration of 5 mM and a circulating flux of 2 mL min<sup>-1</sup> were selected. The deposition time was also a critical parameter for ensuring total coverage of the Cu wires by ZnO nanowires as well as for controlling the ZnO nanowire diameter. ZnO nanowires are not compact structures; therefore, the formation of a free and accessible Cu surface between the nanowires might be possible despite the ZnO nanowires covering the entire surface of the Cu wires.

As shown in Fig. 1, after 30 min of deposition, 86% of the Cu wire surface was covered with ZnO nanocrystals having diameter of 110–190 nm. After 60 min, well-defined ZnO nanowires with diameters of 60–90 nm covered the entire surface of the Cu cables. With a longer deposition time (90 min), well-defined ZnO nanowires were observed, but having diameters of 70–190 nm because of the later growth, which reduced the surface area. Based on these results, the optimum conditions for the synthesis of hairy ZnO@ZnS core@shell Cu cables included a deposition time of 60 min, a zinc nitrate concentration of 5 mM, and a circulating flux of 2 mL min<sup>-1</sup>. The volume of the ZnO deposition solution circulating during ZnO deposition was set to 1 L and the total amount of Cu cables to 9.7552 g of Cu (length of each Cu cable = 52 cm). The volume and Cu substrate were also critical parameters to be considered for the scaling-up of the process. Thus,



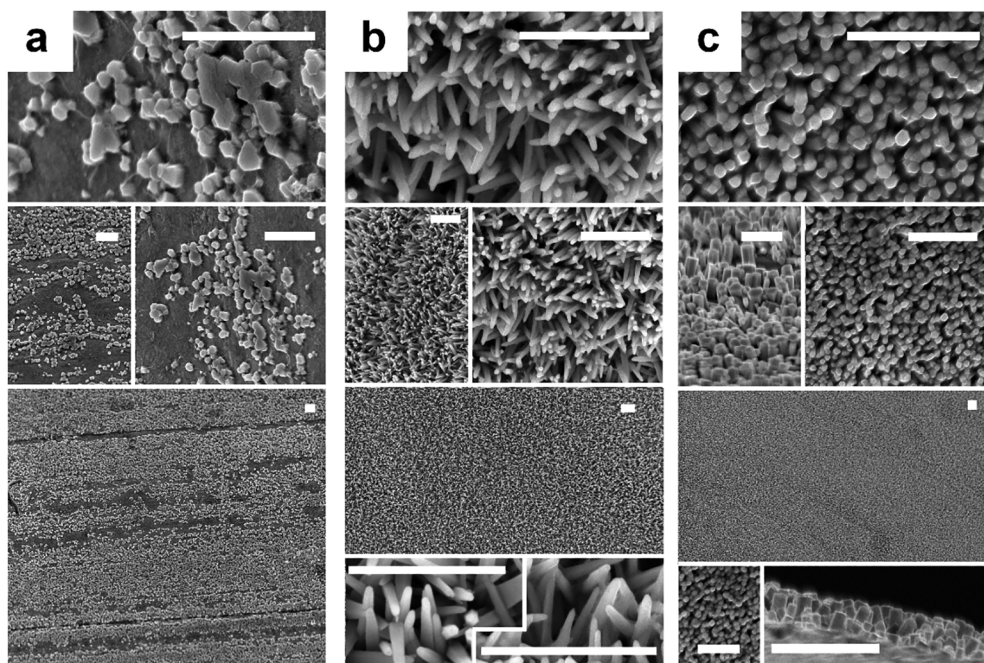


Fig. 1. FE-SEM micrographs of ZnO nanowires on Cu wires after (a) 30 min, (b) 60 min, and (c) 90 min of deposition. Scale bar: 1  $\mu\text{m}$ .

optimized conditions were determined for a novel, simple, inexpensive, green, and scalable strategy for the direct synthesis and integration of ZnO nanowires on Cu cables in silicone tubes (Fig. 1b).

The relatively large band gap ( $E_g = 3.36$  eV), rapid recombination rate of electron-hole pairs, and high photocorrosion activity of ZnO are widely known to inhibit its photocatalytic activity, and consequently, its potential for use in sunlight-driven water decontamination [16,43–46]. However, the band gap of ZnO photocatalysts can be narrowed to fit within the visible region by the formation of ZnO@ZnS core@shell heterostructures, which greatly influence the effective photoresponsive charge separation, improve the carrier mobility, and enhance the photocorrosion resistance, thus significantly improving the sunlight-driven photocatalytic potential for water decontamination [16,47]. To extend the potential applicability of this process, hairy ZnO@ZnS core@shell Cu cables were synthesized by subjecting the well-defined hairy ZnO Cu cables to a sulfidation process.

As shown in Fig. 2, the deposition of ZnO nanowires on Cu cables and the subsequent sulfidation can be readily identified by the naked eye, as the color of the Cu wires changes to brown and then black. The sulfidation process did not appear to affect the architecture of the hairy ZnO Cu cables (Fig. 2b and c) as no changes were observed in the morphology, while the BET surface areas were virtually identical (Fig. S3). The hairy architecture provided a large active surface area (i.e. 87.8 and 90.1  $\text{m}^2 \text{g}^{-1}$  for ZnO and ZnO@ZnS Cu cables, respectively), which was expected to provide enhanced photocatalytic performance for sunlight-driven water decontamination compared to other ZnO-based photocatalysts. The successful sulfidation process was confirmed by changes in the photocatalyst color, energy dispersive spectroscopy and XPS analysis, and XRD characterization.

To gain an insight into the chemical state of the synthesized hairy ZnO and ZnO@ZnS core@shell Cu cables, XPS was performed. Fig. 3a shows the high-resolution XPS spectra of Zn 2p, O 1s, and S 2p. The binding energies obtained from the XPS analysis were corrected by referencing the C 1s to 284.60 eV. The Zn 2p spectra was composed of 2 peaks at 1044.7 and 1021.7 eV, corresponding to the Zn 2p<sub>1/2</sub> and Zn 2p<sub>3/2</sub>, respectively, indicating a normal state of Zn<sup>2+</sup> in both ZnO and ZnO@ZnS photocatalysts. The O 1s spectra of the ZnO Cu cables clearly shows the superposition of three peaks, located at approximately 530.0, 531.9, and 533.1 eV. The low binding energy peak located at 530.0 eV

is attributed to the O<sup>2-</sup> ions in the wurtzite structure of a hexagonal Zn<sup>2+</sup> ion; that located at 531.9 eV is associated with the oxygen vacancies in the matrix of ZnO, while that located at 533.1 eV is generally associated with the presence of chemical-adsorbed hydroxyls or oxygen on the photocatalyst surface. After the sulfidation, only two peaks (centered at 531.8 and 533.1 eV) were observed, which can be associated with the oxygen vacancies and chemical-adsorbed oxygen on the photocatalyst surface. Importantly, the peak observed at approximately 530.0 eV is totally suppressed which is consistent with the formation of a ZnS shell. In addition, the formation of a ZnS layer is clearly confirmed by the S 2p XPS spectra, in which the contributions of the S 2p<sub>1/2</sub> and S 2p<sub>3/2</sub> peaks centered at 162.6 and 161.3 eV, respectively, were observed.

The corresponding XRD patterns of the Cu wires, and hairy ZnO and ZnO@ZnS core@shell Cu cables are shown in Fig. 3b. As expected, the Cu wires were polycrystalline, exhibiting three diffraction peaks at  $2\theta$  values of 43.6, 50.8, and 74.4° corresponding to (111), (200), and (220) planes, matching those of the standard powder diffraction card of Cu (JCPDS card No. 04–0836). For ZnO Cu cables, the principal diffraction peaks appeared at  $2\theta = 31.79^\circ$  (100),  $34.42^\circ$  (002),  $36.25^\circ$  (101),  $47.55^\circ$  (102),  $56.60^\circ$  (110),  $62.86^\circ$  (103),  $66.35^\circ$  (200), and  $67.96^\circ$  (112), which are in agreement with the Miller indices of the crystallographic planes of the standard wurtzite ZnO structure (JCPDS card No. 36-1451). However, three peaks at  $2\theta$  values of 43.6°, 50.8°, and 74.40°, corresponding to the Cu wires, were also detected. No characteristic peaks arising from the impurity phases were observed in the XRD pattern. For the ZnO@ZnS core@shell Cu cables, two extra peaks appeared at  $2\theta = 28.55^\circ$  (111) and  $33.87^\circ$  (200), arising from the cubic ZnS blende structure (JCPDS card No. 65-1691). Note that the strong diffraction peak (002) at  $2\theta = 34.4^\circ$  confirmed preferential the growth of ZnO along the c-axis, which was coherent with the nanowire shape.

The optoelectronic properties of hairy ZnO@ZnS core@shell Cu cables were analyzed to confirm that the formation of a ZnS shell enhanced the UV and visible light absorption properties of ZnO nanowires. As expected, the UV–vis diffuse reflectance spectra (DRS) of the hairy ZnO Cu cables (Fig. 4a) exhibited a strong absorption in the UV region and small absorption intensity in the visible domain. Due to the sulfidation process, the absorption band was displaced to the visible

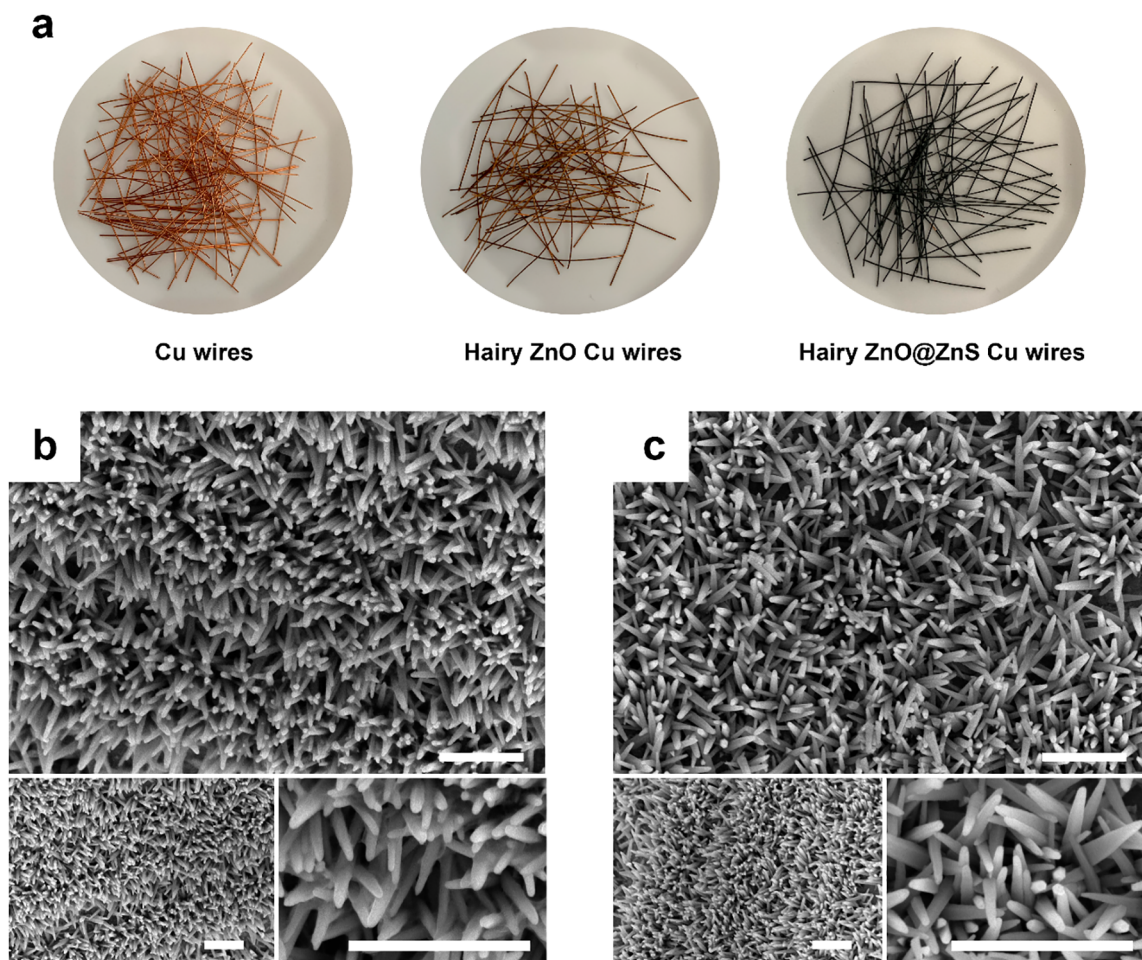


**Fig. 2.** (a) Image of Cu cables, hairy ZnO Cu cables, and hairy ZnO@ZnS core@shell Cu cables. FE-SEM micrographs of (b) hairy ZnO Cu cables and (c) hairy ZnO@ZnS core@shell Cu cables. Scale bar: 1  $\mu\text{m}$ .

region and the intensity of this band also increased significantly, confirming that the ZnO@ZnS heterostructures produced a photoresponse in the visible region. The Tauc plots of  $(\alpha h\nu)^2$  vs  $h\nu$  were plotted for the calculation of the energy band gap of the ZnO and ZnO@ZnS core@shell Cu cables, which were estimated to be 3.23 and 2.75 eV, respectively. The obtained band gap of ZnO@ZnS core@shell Cu cables is significantly smaller than that of the bulk semiconductors (3.37 and 3.54 eV for ZnO and ZnS, respectively) due to the improved separation of the photogenerated electrons and holes in the ZnO-ZnS coupled systems. The slightly smaller band gap of the ZnO core@shell Cu cables may be due to oxygen vacancy defects. These results highlighted the potential of hairy ZnO@ZnS core@shell Cu cables for efficient sunlight photocatalysis applications.

The applicability of ZnO-based photocatalysts is determined not only by their visible-light photosensitivity but also their ability to overcome some of their intrinsic drawbacks such as rapid charge recombination and serious photocorrosion. As shown in Fig. 4b, the photoluminescence spectra of ZnO Cu cables showed two emitting bands, consisting of a strong emission centered at approximately 380 nm and a non-depreciable broad photoluminescence band centered at approximately 630 nm. This band was red-shifted compared to those of other ZnO nanostructures, for which the maximum is generally centered at 550 nm. This red-shift is normally attributed to the presence of oxygen vacancy defects [16,45,51–53]. The photoluminescence spectra of the ZnO@ZnS core@shell Cu cables showed a weak emitting band in the visible region, which could be due to the superposition of bands arising from various individual emissions from the core-shell structure. The formation of a ZnS thin shell on the ZnO nanowires

clearly suppressed the violet emission of the ZnO nanowires, centered at around 380 nm. The weak broad emission centered at 640 nm for the ZnO@ZnS core@shell Cu cables suggested that the ZnO-ZnS interface could reduce the total band gap of the system as well as efficiently decrease the recombination rate of photoinduced charge carriers.

### 3.2. Photocatalytic activity of hairy ZnO@ZnS core@shell Cu cables

The large effective surface area and optoelectronic properties of hairy ZnO and ZnO@ZnS core@shell Cu cables offer great potential for application to water decontamination. The photocatalytic performance was evaluated by performing the photocatalytic mineralization of a single-pollutant solution of MB and a multi-pollutant solution of MB + 4-NP + Rh B under artificial UV-filtered sunlight. Control photolysis (i.e. irradiation in the absence of a photocatalyst) experiments demonstrated negligible mineralization in the absence of a photocatalyst (Fig. S4).

The single-pollutant solution was also used to analyze the adsorption and kinetic properties of the hairy ZnO and ZnO@ZnS core@shell Cu cables. The adsorption-desorption equilibrium of MB was reached after 1 h of circulating the single-pollutant solution under dark conditions. The adsorption of MB was 13–15% for both the hairy ZnO and ZnO@ZnS core@shell Cu cables. After reaching the adsorption-desorption equilibrium of MB, the irradiation of the photocatalysts started and the photocatalytic degradation of MB was monitored by measuring the real-time UV-vis absorption of MB at 662 nm, as shown in Figs. 4 and S5.

Under these conditions, with a flow rate of 0.25 L  $\text{min}^{-1}$ , the hairy

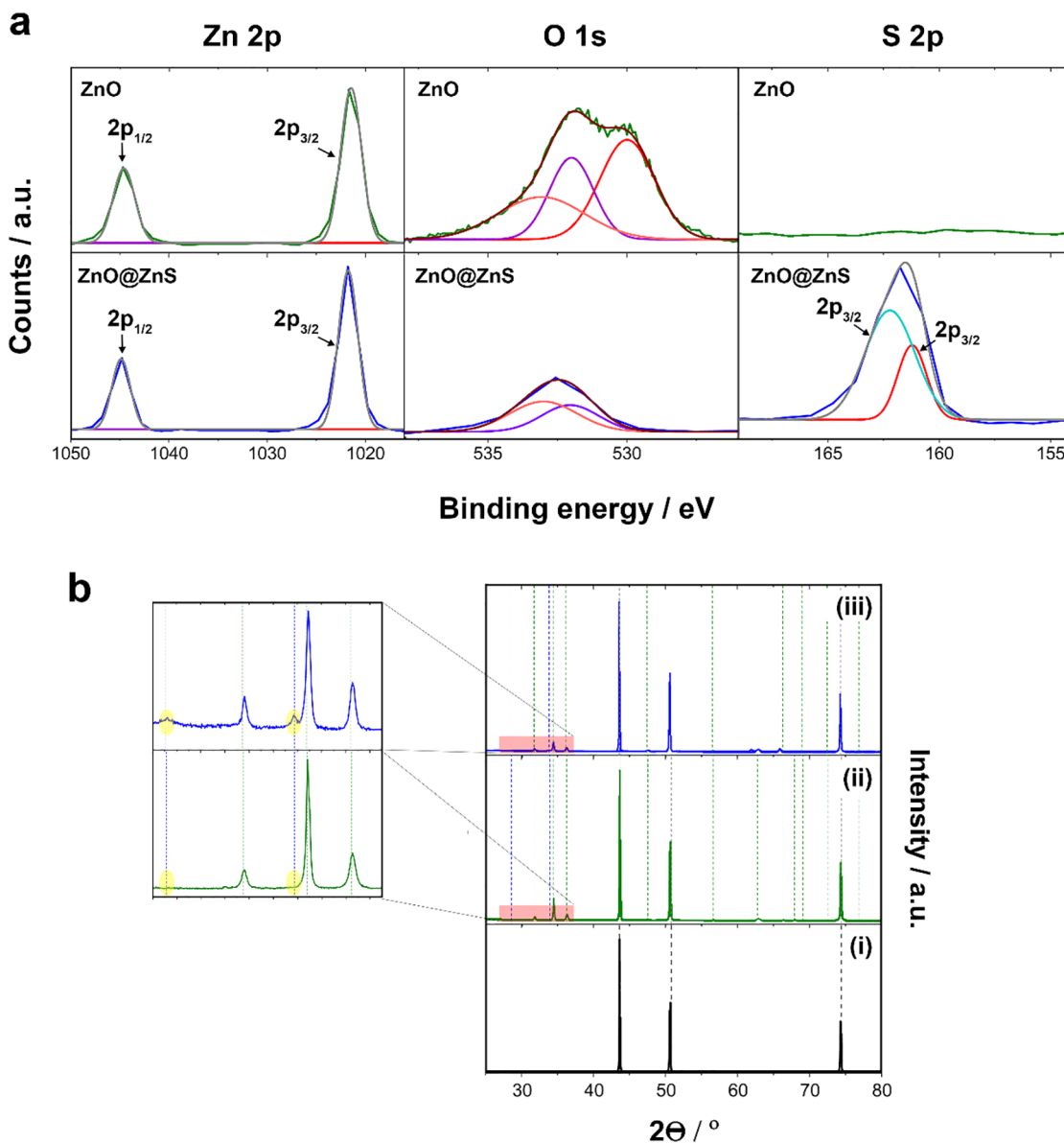


Fig. 3. (a) XPS spectra of Zn 2p, O 1s, and S 2p of hairy ZnO and ZnO@ZnS core@shell Cu cables. (b) XRD pattern of (i) Cu cables, and hairy (ii) ZnO and (iii) ZnO@ZnS core@shell Cu cables.

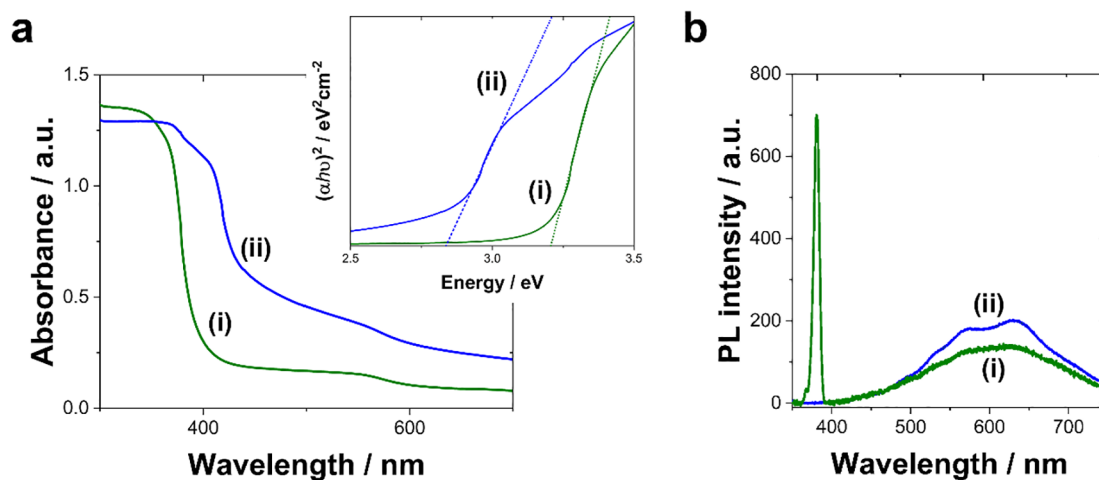
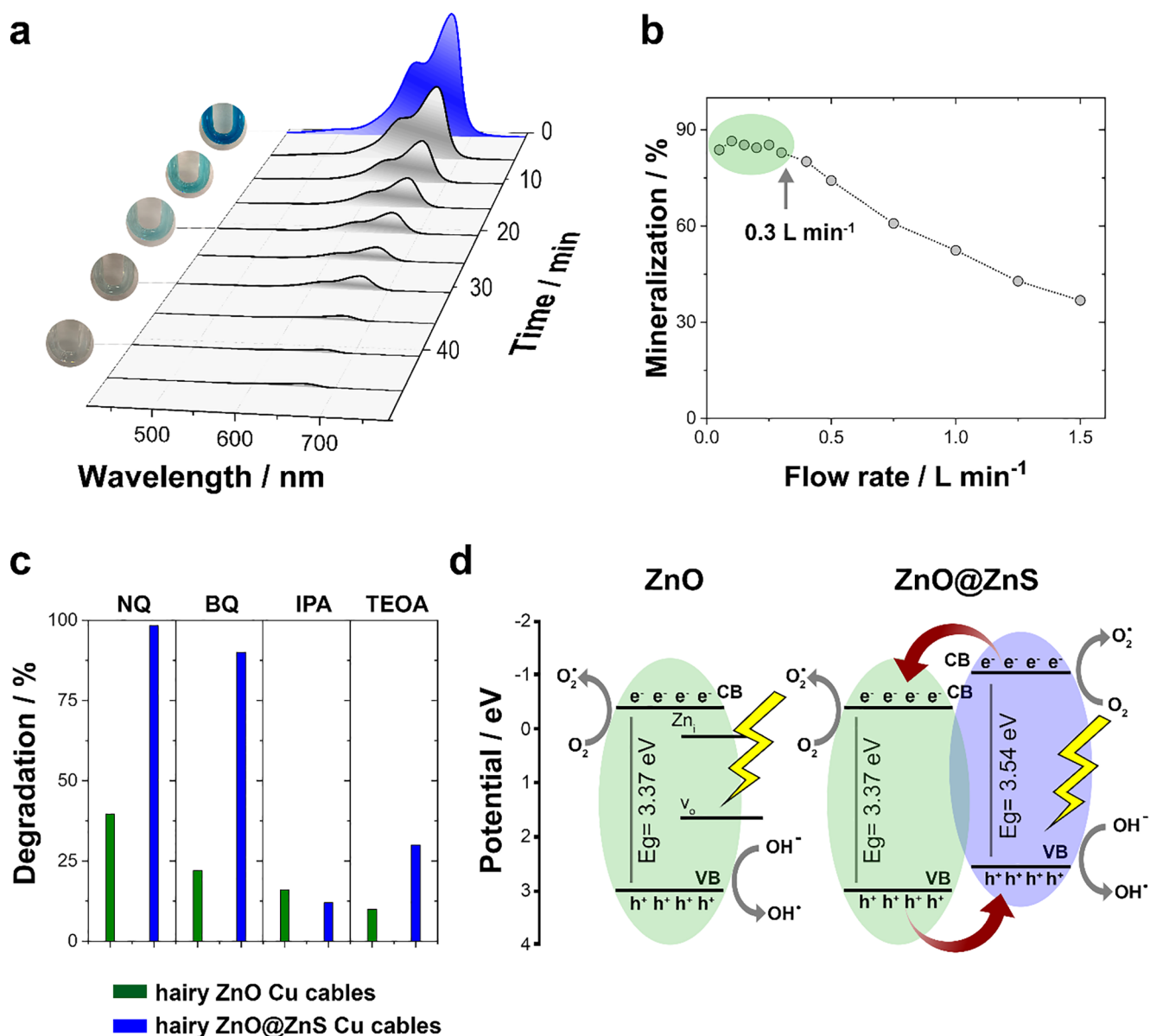


Fig. 4. (a) UV-Vis DRS absorption spectra (inset: Tauc plots from the UV-vis analysis) and (b) room temperature photoluminescence spectra of hairy (i) ZnO and (ii) ZnO@ZnS core@shell Cu cables.





**Fig. 5.** (a) Time-dependent UV-vis spectra of MB photocatalyzed degradation under artificial UV-filtered sunlight ( $\lambda > 400$  nm) using hairy ZnO@ZnS core@shell Cu cables at a concentration of  $0.35 \text{ g L}^{-1}$ , along with images of the circulating MB solution (flux rate =  $0.25 \text{ L min}^{-1}$ ) at different times. (b) Mineralization at different flux rates after 45 min of irradiation under artificial UV-filtered sunlight ( $\lambda > 400$  nm) using hairy ZnO@ZnS core@shell Cu cables ( $0.35 \text{ g L}^{-1}$ ). (c) Trapping experiment of active species during the MB photocatalytic degradation under sunlight ( $\lambda > 400$  nm) using hairy ZnO@ZnS core@shell Cu cables at a concentration of  $0.35 \text{ g L}^{-1}$  and a flux rate of  $0.25 \text{ L min}^{-1}$ . NQ, BQ, IPA, and TEOA are used to indicate non-quencher and benzoquinone, isopropyl alcohol, and triethanolamine quenchers, respectively. (d) Schematic representation of the photocatalytic mechanism of hairy ZnO@ZnS core@shell Cu cables.

**Table 1**

BET surface areas of hairy ZnO and ZnO@ZnS core@shell Cu cables, light intensity, photocatalytic degradation (%), mass-normalized kinetic constants, and mineralization (%) of MB (10 ppm) for pollutant solutions under artificial UV-filtered sunlight ( $\lambda > 400$  nm) using hairy ZnO and ZnO@ZnS core@shell Cu cables ( $0.35 \text{ g L}^{-1}$ ). The values of light source intensity depicted in this table correspond to the average intensity values on the photocatalyst's surface (i.e., inside the silicone tubes) – 23% of light intensity was absorbed by the silicone tubes (i.e., the light intensity on the external silicone tubes was approximately 580 lx).

Photocatalyst	ZnS to ZnO/at. %	BET surface area/ $\text{m}^2 \text{ g}^{-1}$	Light source intensity/lx ( $\lambda > 400$ nm)	Flux rate/L $\text{min}^{-1}$	Photocatalytic degradation (45 min) /%	Mass-normalized kinetic constant/ $\text{min}^{-1} \text{ g}^{-1}$	Mineralization /% (45 min)
ZnO	–	87.8	$450 \pm 20$ lx	0.25	$39.6 \pm 0.8$	0.02	$31.2 \pm 0.5$
ZnO@ZnS	$10.2 \pm 0.8$	90.1	$450 \pm 20$ lx	0.25	$98.3 \pm 0.4$	0.13	$85.3 \pm 0.3$

ZnO Cu cables exhibited a MD photocatalytic degradation level of 39% after 45 min of artificial UV-filtered sunlight irradiation (Fig. S5), which was significantly smaller than the 98% photocatalytic degradation obtained with the hairy ZnO@ZnS core@shell Cu cables (Fig. 5a).

As shown in Fig. 5a, the photocatalytic degradation of MB was visually observed due to the decoloration of the initial methylene blue solution. However, the mineralization, as measured by the TOC reduction, was relatively small as values of 31% and 85% (Table 1) were achieved for



the hairy ZnO and ZnO@ZnS core@shell Cu cables, respectively, over a time period of 45 min. Importantly, for hairy ZnO@ZnS core@shell Cu cables, complete TOC removal (i.e., mineralization > 99%) occurred after time period of 65 min. Note that the total mineralization of organic pollutants is a critical parameter as some intermediates may be equal or more harmful than the initial contaminant.

According to the Langmuir–Hinshelwood model, at low concentrations, MB degradation obeys pseudo first-order kinetics with respect to the MB concentration. Consequently, the apparent kinetic rate constant could be calculated from a plot of the logarithm of the absorbance [ $-\ln(A_t/A_0)$ ] as a function of the reaction time (Fig. S6) and normalized by the mass of the photocatalyst to compare the photocatalytic activity of hairy ZnO@ZnS core@shell Cu cables and state-of-the-art ZnO-based photocatalysts [8,48–50,54,55]. This mass-normalized reaction rate constant (Table 1) of the ZnO@ZnS core@shell Cu cables was almost 6.5 times higher than that of the hairy ZnO Cu cables. The mass-normalized kinetic rate constants under non-circulating conditions (reaction volume = 20 mL, photocatalyst dosage =  $0.35 \text{ g L}^{-1}$ , magnetic stirring = 200 rpm) for the hairy ZnO and ZnO@ZnS core@shell Cu cables were 2.1 and  $14.3 \text{ min}^{-1} \text{ g}^{-1}$ , respectively. These values are not comparable since in non-circulating conditions and small volumes, but under magnetic stirring (400 rpm), both the pollutant-photocatalyst and light-photocatalyst interactions are higher. The development of a tubular continuous flow reactor, especially when large volumes of industrial wastewater are to be handled, requires an analysis of the role of the flow rate on the overall photocatalytic performance. The experimental work was limited to low flow rates, ranging from 0.05 to  $1.5 \text{ L min}^{-1}$ . However, the general behavior can be extracted from these experiments. As shown in Fig. 5b, the mineralization of MB for hairy ZnO and ZnO@ZnS core@shell Cu cables was virtually constant until a flow rate of  $0.3 \text{ L min}^{-1}$  was exceeded. In the studied range, the increase in the flow rate was translated into a reduction in the mineralization. Because of the complexity of the photocatalytic mineralization process, which requires pollutant adsorption and multiple oxidation reactions, it is thought that the low flow rates resulted in improved global mineralization results.

The significantly enhanced photocatalytic activity of the ZnO@ZnS core@shell Cu cables prompted further investigation of the photocatalytic reaction mechanism of the degradation process. To investigate the role of hydroxyl radicals, superoxide radicals, and photogenerated holes in the degradation process, trapping experiments were performed (Fig. 5c). For the ZnO Cu cables, the photocatalytic degradation (39%), after 45 min of artificial UV-filtered sunlight irradiation, decreased to ~22%, ~16%, and ~30%, in the presence of superoxide radical (i.e., BQ), hydroxyl radical (i.e., IPA), and hole (i.e., TEOA) scavengers, respectively. These results suggested that the production of superoxide and hydroxyl radicals governed the degradation of MB when the ZnO Cu cables were used. On the other hand, the photocatalytic degradation of MB was governed by the photogenerated holes and the hydroxyl radicals when the ZnO@ZnS core@shell Cu cables were used as photocatalysts. The degradation of the ZnO@ZnS core@shell Cu cables (~99%) decreased to ~90%, ~12%, and ~10% in the presence of superoxide radicals, hydroxyl radicals, and hole quenchers, respectively. In summary, under UV-filtered sunlight irradiation the superoxide radicals and hydroxyl radicals play a more significant role than holes in the case of the ZnO Cu cables, whereas the holes and hydroxyl radicals are more significant than the superoxide radicals for the ZnO@ZnS core@shell Cu cables.

Based on the above experimental results, a possible mechanism (Fig. 5d) is proposed for the UV-filtered sunlight irradiation of hairy ZnO and ZnO@ZnS core@shell Cu cables. Photoinduced electrons and holes cannot be produced under UV-filtered sunlight irradiation when pure ZnO and ZnS are used due to their wide band gap (3.37 and 3.54 eV for ZnO and ZnS, respectively) [56,57]. However, experimental and theoretical studies demonstrated that the formation of ZnO@ZnS core@shell interfaces leads to important diminution in the band gap

energy of the system due to the interfacial lattice strain that occurs along the interface of the type II ZnO-ZnS heterostructures [8,18,43–45,47]. As shown in Fig. 5d, at the interface of the ZnO-ZnS heterojunction, the photogenerated electrons could be transferred from the conduction band of the ZnS into the conduction band of the ZnO, whereas the holes could be transferred from the valence band of the ZnO into that of the ZnS. This fact hinders the recombination process of electron-hole (see Fig. 4b) and significantly improves the efficiency of the interfacial charge separation. Such separation is pivotal to trapping the holes at the ZnS/water interface, where the hydroxyl radicals can be efficiently generated. Note that hydroxyl radicals can be generated mainly via the reaction of photogenerated holes with adsorbed water or hydroxyl ions; the reaction of superoxide radicals with protons; and the photolysis of water. Despite the different possible sources of hydroxyl radicals, the photolysis of water and the reaction of superoxide radicals with protons, in neutral or alkaline media, are less important than those obtained via the reaction of photogenerated holes with adsorbed water or hydroxyl ions [43–45,47]. Due to the low oxidation power of superoxide radicals, it is expected that their main function is the formation of hydroxyl radicals upon reacting with protons, which may be more relevant under acidic conditions. Consequently, the exceptional photocatalytic activity of the hairy ZnO@ZnS core@shell Cu cables can be attributed to the combined effects of the improved light trapping efficiency given by the hairy architecture, and the synergistic effect between the ZnO core and ZnS shell, which induces a substantial reduction in the bandgap and the improved separation of the electron-hole pairs.

To determine whether the photocatalytic system designed in this work was suitable for real-life practical purposes, a multi-pollutant solution containing MB, 4-NP, and Rh B was treated using the hairy ZnO@ZnS core@shell Cu cables (Fig. 6 and Fig. S7). The mineralization of 2 L of this solution after 320 min of circulation under UV-filtered sunlight irradiation was found to be equal to 97%. Consequently, the hairy ZnO@ZnS core@shell Cu cables were demonstrated to be a reliable and promising system for the efficient mineralization of persistent organic pollutants or the total/partial oxidation of other emerging pollutants due to their excellent UV-filtered photocatalytic activity as a consequence of their improved light absorption in the visible region and the effective separation of photogenerated electron-hole pairs at the ZnO@ZnS core@shell heterojunctions.

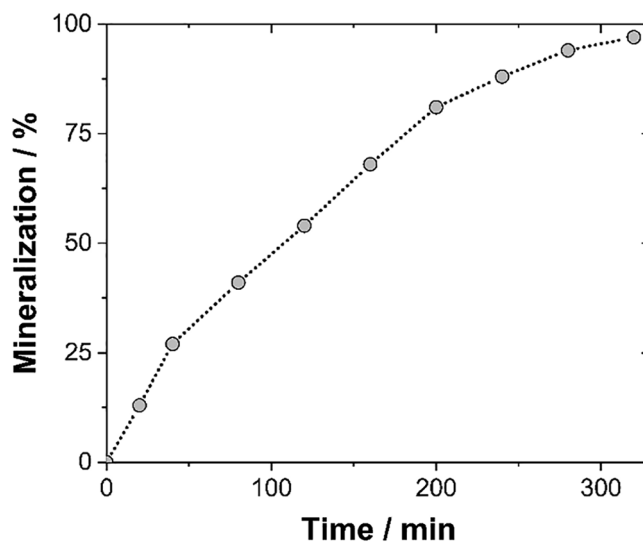
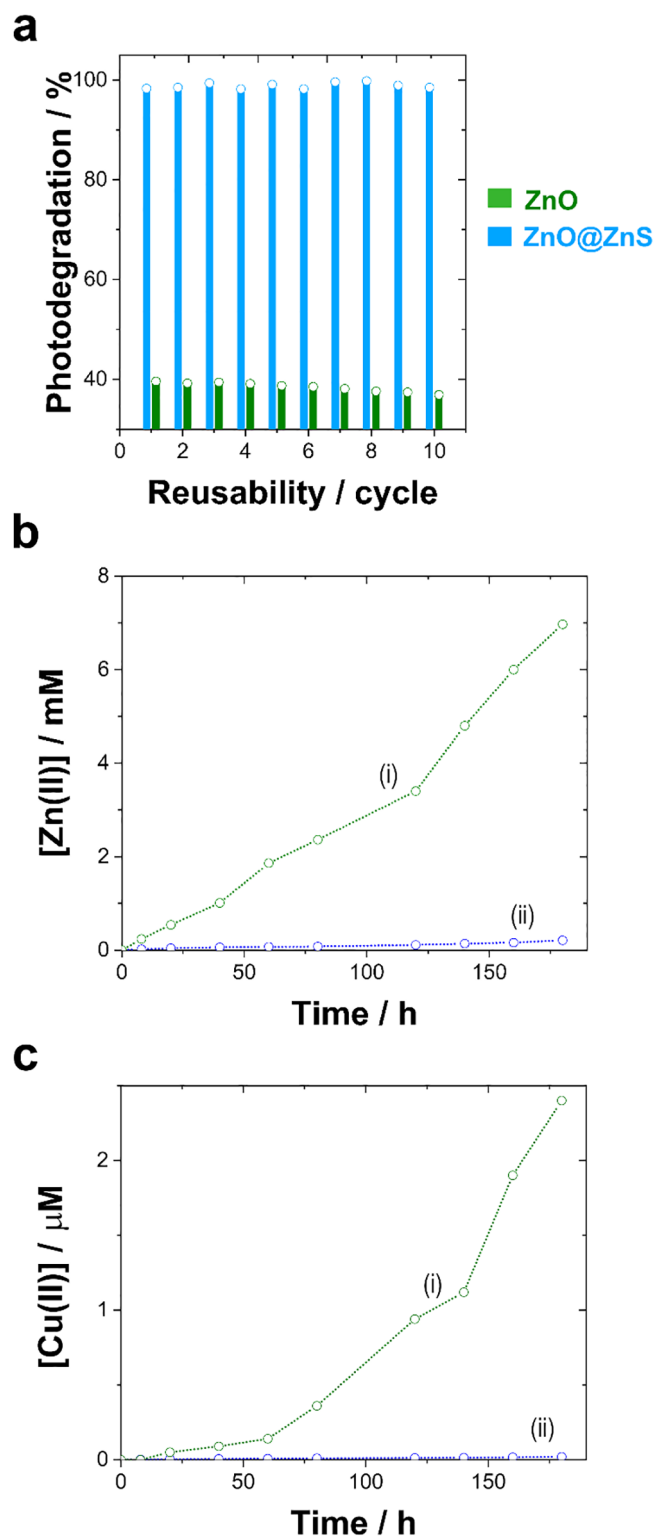


Fig. 6. Mineralization of a multi-pollutant solution containing MB, 4-NP, and Rh B under artificial UV-filtered sunlight ( $\lambda > 400 \text{ nm}$ ) using hairy ZnO@ZnS core@shell Cu cables ( $0.35 \text{ g L}^{-1}$ ) with a flux rate of  $0.25 \text{ L min}^{-1}$ .



**Fig. 7.** (a) Photocatalyst reusability of hairy ZnO and ZnO@ZnS core@shell Cu cables ( $0.35 \text{ g L}^{-1}$ ) in cyclic photocatalytic degradation experiments (45 min) of MB for ten consecutive cycles under artificial UV-filtered sunlight ( $\lambda > 400 \text{ nm}$ ) (flux rate of  $0.25 \text{ L min}^{-1}$ ). Time-dependent concentration of (b) Zn(II) and (c) Cu(II) ions in the circulating water (flux rate of  $0.25 \text{ L min}^{-1}$ ) under artificial UV-filtered sunlight ( $\lambda > 400 \text{ nm}$ ) in the presence of hairy (i) ZnO and (ii) ZnO@ZnS core@shell Cu cables ( $0.35 \text{ g L}^{-1}$ ).

### 3.3. Photostability of hairy ZnO@ZnS core@shell Cu cables

Photostability and reproducibility are other key factors affecting the robustness of photocatalyst synthesis. The reusability was investigated by repeating the photocatalytic degradation experiments of the single-pollutant solution of MB for ten runs. After each run, fresh MilliQ-Millipore water was circulated for 5 min before the reactor was reused for the next run. The integration of a ZnO-based photocatalyst on the Cu cables allowed for the reactor to be reused directly without requiring centrifugation or other methods to recuperate the photocatalyst. As shown in Fig. 7a, the photocatalytic degradation of MB was virtually constant with the hairy ZnO@ZnS core@shell Cu cables. However, a slight reduction in the degradation of the MB was observed after 10 runs with the ZnO Cu cables, likely due to the high photocorrosion activity of ZnO during irradiation.

To further investigate the photostability of hairy ZnO and ZnO@ZnS core@shell Cu cables, time-dependent concentrations of Zn(II) and Cu(II) ions in the circulating water (flux rate of  $0.25 \text{ L min}^{-1}$ ) under 180 h of artificial UV-filtered sunlight irradiation were spectrophotometrically determined (Fig. 7b). As shown in Fig. 6b, hairy ZnO@ZnS core@shell Cu cables exhibited excellent reusability and stability with negligible photocorrosion (i.e. dissolution of photocatalyst  $< 2\%$  after 180 h of continuous irradiation), demonstrating great potential for long-term mineralization of organic pollutants. Despite of Cu cables were completely covered with ZnO@ZnS nanowires, the Cu(II) concentration was also analyzed. Note that the non-compact architecture of nanowires might offer free and accessible Cu surface between the nanowires, and therefore, liquid (and less probably, light) might interact with the accessible Cu surface. However, after the sulfidation process, it would be expected that  $\text{CuS}_x$  would form on the surfaces of the accessible Cu cables. Despite this possibility, there is no experimental evidence to support the surface of the Cu being partially accessible. Importantly, for the hairy ZnO and ZnO@ZnS core@shell Cu cables, Cu(II) could not be detected during irradiation and fluid circulation over 180 h. On the other hand, the hairy ZnO Cu cables exhibited a relatively high photocorrosion activity as non-depreciable concentrations of Zn(II) ions were detected after 180 h of continuous irradiation. Importantly, a small amount of Cu(II) ions was also detected in the micromolar range, which could be attributed to the Cu leaching after the dissolution of ZnO. No structural damage was observed by FE-SEM analysis after the 180 h of continuous irradiation.

### 3.4. Recyclability

The fabrication of new photocatalysts, as well as the design of photocatalytic reactors, should adhere to the twelve principles of green chemistry and the twelve principles of circular chemistry for environmental and sustainable research fields, which include applications such as water decontamination [8,58]. Cleaner production of photocatalysts requires the prevention of the production of waste as well as the enhancement of efficiency in energy, water, resources, and human capital usage. Herein, the recyclability of hairy ZnO@ZnS core@shell Cu cables was explored. After reaching the end of the effective lifetime of hairy ZnO@ZnS core@shell Cu cables, the remaining photocatalyst and Cu substrate were removed and cleaned, respectively, by circulating a  $0.5 \text{ M H}_2\text{SO}_4$  solution through the silicon tube for 15 min. Following this, MilliQ-Millipore water was circulated for 5 min to remove the sulfuric solution, giving freshly recycled Cu wires ready for another round of sequential chemical deposition of ZnO and sulfidation processes to produce fresh hairy ZnO@ZnS core@shell nanowires (Fig. S8). As shown in Fig. S8, well-defined ZnO@ZnS core@shell nanowires were deposited on the recycled Cu cables. Thus, the ability to recover Zn(II) and Cu(II) ions by dissolving with sulfuric acid solution and separate by factorial crystallization is highly favorable for the synthesis of new photocatalysts.

#### 4. Conclusions

A novel, simple, and scalable method for the direct chemical synthesis of hairy ZnO@ZnS core@shell Cu cables, which can be directly integrated into a continuous-flow, tubular-type reactor for continuous sunlight-driven water decontamination, was proposed. This process was demonstrated to be environmentally-friendly and addressed key sustainability concerns, providing a circular strategy that prevented the production of residues and increased the efficiency of usage of the energy, water, chemicals, and other resources. The proposed strategy is expected to be useful for the design of new reactors for continuous water decontamination, as no catalyst separation is required. The obtained hairy ZnO@ZnS core@shell Cu cables exhibited excellent photocatalytic activity (photocatalytic degradation > 99% and mineralization > 99%) under artificial UV-filtered sunlight irradiation due to the increased surface area, improved visible-light absorption, and enhanced separation efficiency of photo-generated electron-hole pairs. The hairy architecture was also pivotal to improve the light trapping capability. The MB degradation rate of hairy ZnO@ZnS core@shell Cu cables ( $14.3 \text{ min}^{-1} \text{ g}^{-1}$  under static conditions and  $0.13 \text{ min}^{-1} \text{ g}^{-1}$  in a dynamic system) was approximately 6.8 times higher than that of pure ZnO ( $2.1 \text{ min}^{-1} \text{ g}^{-1}$  under static conditions and  $0.02 \text{ min}^{-1} \text{ g}^{-1}$  in a dynamic system). The effect of flow rate on the continuous mineralization of MB is also investigated, indicating that low flow rates are more efficient for mineralization of persistent organic pollutants. The formation of a ZnO@ZnS core@shell interface is demonstrated as being crucial to diminishing the global band gap energy of the system due to the interfacial lattice strain that occurs along the interface of the type II ZnO-ZnS heterostructures. This fact is translated into an improvement in the efficiency of the interfacial charge separation, which facilitates the formation of hydroxyl radicals, and minimal photocorrosion activity. The hairy ZnO@ZnS core@shell Cu cables exhibited high stability (photocatalyst dissolution < 2% after 180 h of irradiation) and were able to be utilized over an extended duration, which is possibly the major concern pertaining to scalability. Finally, we demonstrated that the photocatalyst precursors and substrate could be recuperated and reused directly after reaching the end of the photocatalyst lifetime, thus adhering to circular and green chemistry principles for the photocatalyst design.

#### Declaration of Competing Interest

The authors declare that they have no known competing financial interests or personal relationships that could have appeared to influence the work reported in this paper.

#### Acknowledgements

This work was supported by the Metrohm foundation. Albert Serrà would like to acknowledge funding from the EMPAPOSTDOCS-II program. The EMPAPOSTDOCS-II programme has received funding from the European Union's Horizon 2020 research and innovation programme under the Marie Skłodowska-Curie grant agreement number 754364.

#### Appendix A. Supplementary data

Supplementary data to this article can be found online at <https://doi.org/10.1016/j.cej.2020.126164>.

#### References

- [1] UNESCO, Nature-based solutions for water, 2018.
- [2] R. Bain, R. Johnston, F. Mitis, C. Chatterley, T. Slaymaker, Establishing sustainable development goal baselines for household drinking water, sanitation and hygiene services, *Water* (Switzerland). 10 (2018), <https://doi.org/10.3390/w10121711>.
- [3] E. Brillas, C.A. Martínez-Huitle, Decontamination of wastewaters containing synthetic organic dyes by electrochemical methods. An updated review, *Appl. Catal. B Environ.* 166–167 (2015) 603–643, <https://doi.org/10.1016/j.apcatb.2014.11.016>.
- [4] G. Ferro, A. Fiorentino, M.C. Alferez, M.I. Polo-López, L. Rizzo, P. Fernández-Ibañez, Urban wastewater disinfection for agricultural reuse: effect of solar driven AOPs in the inactivation of a multidrug resistant *E. coli* strain, *Appl. Catal. B Environ.* 178 (2015) 65–73, <https://doi.org/10.1016/j.apcatb.2014.10.043>.
- [5] M. Clara, B. Strenn, O. Gans, E. Martínez, N. Kreuzinger, H. Kroiss, Removal of selected pharmaceuticals, fragrances and endocrine disrupting compounds in a membrane bioreactor and conventional wastewater treatment plants, *Water Res.* 39 (2005) 4797–4807, <https://doi.org/10.1016/j.watres.2005.09.015>.
- [6] A. Serrà, P. Pip, E. Gómez, L. Philippe, Efficient magnetic hybrid ZnO-based photocatalysts for visible-light-driven removal of toxic cyanobacteria blooms and cyanotoxins, *Appl. Catal. B Environ.* 268 (2020) 118745, <https://doi.org/10.1016/j.apcatb.2020.118745>.
- [7] C. Grandclément, I. Seyssiecq, A. Piram, P. Wong-Wah-Chung, G. Vanot, N. Tiliacos, N. Roche, P. Doumenq, From the conventional biological wastewater treatment to hybrid processes, the evaluation of organic micropollutant removal: a review, *Water Res.* 111 (2017) 297–317, <https://doi.org/10.1016/j.watres.2017.01.005>.
- [8] A. Serrà, R. Artal, J. García-Amorós, B. Sepúlveda, E. Gómez, J. Nogués, L. Philippe, Hybrid Ni@ZnO@ZnS-microalgae for circular economy: a smart route to the efficient integration of solar photocatalytic water decontamination and bioethanol production, *Adv. Sci.* 7 (2020) 1–9, <https://doi.org/10.1002/advs.201902447>.
- [9] F.C. Moreira, R.A.R. Boaventura, E. Brillas, V.J.P. Vilar, Electrochemical advanced oxidation processes: a review on their application to synthetic and real wastewaters, *Appl. Catal. B Environ.* 202 (2017) 217–261, <https://doi.org/10.1016/j.apcatb.2016.08.037>.
- [10] K.M. Lee, C.W. Lai, K.S. Ngai, J.C. Juan, Recent developments of zinc oxide based photocatalyst in water treatment technology: a review, *Water Res.* 88 (2016) 428–448, <https://doi.org/10.1016/j.watres.2015.09.045>.
- [11] V. Etacheri, C. Di Valentin, J. Schneider, D. Bahnemann, S.C. Pillai, Visible-light activation of TiO<sub>2</sub> photocatalysts: advances in theory and experiments, *J. Photochem. Photobiol. C Photochem. Rev.* 25 (2015) 1–29, <https://doi.org/10.1016/j.jphotochemrev.2015.08.003>.
- [12] D. Spasiano, R. Marotta, S. Malato, P. Fernandez-Ibañez, I. Di Somma, Solar photocatalysis: materials, reactors, some commercial, and pre-industrialized applications. A comprehensive approach, *Appl. Catal. B Environ.* 170–171 (2015) 90–123, <https://doi.org/10.1016/j.apcatb.2014.12.050>.
- [13] Y. Li, Y. Bu, F. Jiang, X. Dai, J.P. Ao, Fabrication of ultra-sensitive photoelectrochemical aptamer biosensor: based on semiconductor/DNA interfacial multifunctional reconciliation via 2D–C3N<sub>4</sub>, *Biosens. Bioelectron.* 150 (2020) 111903, <https://doi.org/10.1016/j.bios.2019.111903>.
- [14] M. Birnie, S. Riffat, M. Gillott, Photocatalytic reactors: design for effective air purification, *Int. J. Low-Carbon Technol.* 1 (2006) 47–58, <https://doi.org/10.1093/ijlct/1.1.47>.
- [15] A. Visan, J.R. Van Ommen, M.T. Kreuzer, R.G.H. Lammertink, Photocatalytic Reactor Design: Guidelines for Kinetic Investigation, *Ind. Eng. Chem. Res.* 58 (2019) 5349–5357, <https://doi.org/10.1021/acs.iecr.9b00381>.
- [16] S. Banerjee, S.C. Pillai, P. Falaras, K.E. O'shea, J.A. Byrne, D.D. Dionysiou, New Insights into the Mechanism of Visible Light Photocatalysis, *J. Phys. Chem. Lett.* 5 (2014) 2543–2554, <https://doi.org/10.1021/jz501030x>.
- [17] F. Fresno, R. Portela, S. Suárez, J.M. Coronado, Photocatalytic materials: recent achievements and near future trends, *J. Mater. Chem. A.* 2 (2014) 2863–2884, <https://doi.org/10.1039/c3ta13793g>.
- [18] A. Serrà, Y. Zhang, B. Sepúlveda, E. Gómez, J. Nogués, J. Michler, L. Philippe, Highly active ZnO-based biomimetic fern-like microleaves for photocatalytic water decontamination using sunlight, *Appl. Catal. B Environ.* 248 (2019) 129–146, <https://doi.org/10.1016/j.apcatb.2019.02.017>.
- [19] M.R. Hoffmann, S.T. Martin, W. Choi, D.W. Bahnemann, Environmental applications of semiconductor photocatalysis, *Chem. Rev.* 95 (1995) 69–96, <https://doi.org/10.1021/cr00033a004>.
- [20] P.S. Mukherjee, A.K. Ray, Major challenges in the design of a large-scale photocatalytic reactor for water treatment, *Chem. Eng. Technol.* 22 (1999) 253–260, [https://doi.org/10.1002/\(sici\)1521-4125\(199903\)22:3<253::aid-ecat253>3.0.co;2-x](https://doi.org/10.1002/(sici)1521-4125(199903)22:3<253::aid-ecat253>3.0.co;2-x).
- [21] S. Garcia-Segura, E.B. Cavalcanti, E. Brillas, Mineralization of the antibiotic chloramphenicol by solar photoelectro-Fenton. From stirred tank reactor to solar pre-pilot plant, *Appl. Catal. B Environ.* 144 (2014) 588–598, <https://doi.org/10.1016/j.apcatb.2013.07.071>.
- [22] I.F.J. Vankelcom, Polymeric membranes in catalytic reactors, *Chem. Rev.* 102 (2002) 3779–3810, <https://doi.org/10.1021/cr0103468>.
- [23] C. McCullagh, N. Skillen, M. Adams, P.K.J. Robertson, Photocatalytic reactors for environmental remediation: a review, *J. Chem. Technol. Biotechnol.* 86 (2011) 1002–1017, <https://doi.org/10.1002/jctb.2650>.
- [24] R.J. Braham, A.T. Harris, Review of major design and scale-up considerations for solar photocatalytic reactors, *Ind. Eng. Chem. Res.* 48 (2009) 8890–8905, <https://doi.org/10.1021/ie900859z>.
- [25] K. Natarajan, T.S. Natarajan, H.C. Bajaj, R.J. Tayade, Photocatalytic reactor based on UV-LED/TiO<sub>2</sub> coated quartz tube for degradation of dyes, *Chem. Eng. J.* 178 (2011) 40–49, <https://doi.org/10.1016/j.cej.2011.10.007>.
- [26] M.F.J. Dijkstra, H. Buwalda, A.W.F. De Jong, A. Michorius, J.G.M. Winkelman, A.A.C.M. Beenackers, Experimental comparison of three reactor designs for photocatalytic water purification, *Chem. Eng. Sci.* 56 (2001) 547–555, [https://doi.org/10.1016/S0009-2509\(00\)00259-1](https://doi.org/10.1016/S0009-2509(00)00259-1).
- [27] D.A. Keane, K.G. McGuigan, P.F. Ibañez, M.I. Polo-López, J.A. Byrne, P.S.M. Dunlop, K. O'Shea, D.D. Dionysiou, S.C. Pillai, Solar photocatalysis for water



- disinfection: materials and reactor design, *Catal. Sci. Technol.* 4 (2014) 1211–1226, <https://doi.org/10.1039/c4cy00006d>.
- [28] K. Song, M. Mohseni, F. Taghipour, Application of ultraviolet light-emitting diodes (UV-LEDs) for water disinfection: a review, *Water Res.* 94 (2016) 341–349, <https://doi.org/10.1016/j.watres.2016.03.003>.
- [29] T.S. Natarajan, K. Natarajan, H.C. Bajaj, R.J. Tayade, Energy efficient UV-LED source and TiO<sub>2</sub> nanotube array-based reactor for photocatalytic application, *Ind. Eng. Chem. Res.* 50 (2011) 7753–7762, <https://doi.org/10.1021/ie200493k>.
- [30] P. Dhandapani, A.A. Prakash, M.S. AlSalhi, S. Maruthamuthu, S. Devanesan, A. Rajasekar, Ureolytic bacteria mediated synthesis of hairy ZnO nanostructure as photocatalyst for decolorization of dyes, *Mater. Chem. Phys.* 243 (2020) 122619, <https://doi.org/10.1016/j.matchemphys.2020.122619>.
- [31] S. Xu, Z.L. Wang, One-dimensional ZnO nanostructures: Solution growth and functional properties, *Nano Res.* 4 (2011) 1013–1098, <https://doi.org/10.1007/s12274-011-0160-7>.
- [32] Q. Li, V. Kumar, Y. Li, H. Zhang, T.J. Marks, R.P.H. Chang, Fabrication of ZnO nanorods and nanotubes in aqueous solutions, *Chem. Mater.* 17 (2005) 1001–1006, <https://doi.org/10.1021/cm048144q>.
- [33] Y. Tak, K. Yong, Controlled growth of well-aligned ZnO nanorod array using a novel solution method, *J. Phys. Chem. B.* 109 (2005) 19263–19269, <https://doi.org/10.1021/jp0538767>.
- [34] N. Saito, H. Haneda, K. Koumoto, Influences of growth conditions to morphology of ZnO thin films electrolessly deposited on Pd catalyst, *J. Cer. Soc. Jpn.* 115 (2007) 850–855, <https://doi.org/10.2109/jcersj.2.115.850>.
- [35] N. Saito, H. Haneda, T. Sekiguchi, N. Ohashi, I. Sakaguchi, K. Koumoto, Low-temperature fabrication of light-emitting zinc oxide micropatterns using self-assembled monolayers, *Adv. Mater.* 14 (2002) 418–421, [https://doi.org/10.1002/1521-4095\(20020318\)14:6<418::aid-adma418>3.0.co;2-k](https://doi.org/10.1002/1521-4095(20020318)14:6<418::aid-adma418>3.0.co;2-k).
- [36] T. Shinagawa, S. Otomo, J. Ichi Katayama, M. Izaki, Electroless deposition of transparent conducting and <0 0 0 1>-oriented ZnO films from aqueous solutions, *Electrochim. Acta.* 53 (2007) 1170–1174, <https://doi.org/10.1016/j.electacta.2007.03.056>.
- [37] D. Plana, A.I. Campbell, S.N. Patole, G. Shul, R.A.W. Dryfe, Kinetics of electroless deposition: The copper-dimethylamine borane system, *Langmuir.* 26 (2010) 10334–10340, <https://doi.org/10.1021/la100390x>.
- [38] T. Homma, A. Tamaki, H. Nakai, T. Osaka, Molecular orbital study on the reaction process of dimethylamine borane as a reductant for electroless deposition, *J. Electroanal. Chem.* 559 (2003) 131–136, [https://doi.org/10.1016/S0022-0728\(03\)00042-1](https://doi.org/10.1016/S0022-0728(03)00042-1).
- [39] T. Shinagawa, H. Takahashi, M. Izaki, Direct growth of ZnO crystals on various Cu substrates by Cu-catalyzed chemical bath deposition, *CrystEngComm.* 21 (2019) 2476–2480, <https://doi.org/10.1039/C9CE00244H>.
- [40] C.E. Säbel, J.M. Neureuther, S. Siemann, A spectrophotometric method for the determination of zinc, copper, and cobalt ions in metalloproteins using Zincon, *Anal. Biochem.* 397 (2010) 218–226, <https://doi.org/10.1016/j.ab.2009.10.037>.
- [41] D. Fu, D. Yuan, Spectrophotometric determination of trace copper in water samples with thiomichlersketone, *Spectrochim. Acta – Part A Mol. Biomol. Spectrosc.* 66 (2007) 434–437, <https://doi.org/10.1016/j.saa.2006.03.018>.
- [42] M.J. Ahmed, M.N. Uddin, A simple spectrophotometric method for the determination of cobalt in industrial, environmental, biological and soil samples using bis (salicylaldehyde)orthophenylenediamine, *Chemosphere.* 67 (2007) 2020–2027, <https://doi.org/10.1016/j.chemosphere.2006.11.020>.
- [43] A. Serrà, E. Gómez, L. Philippe, Bioinspired ZnO-based solar photocatalysts for the efficient decontamination of persistent organic pollutants and hexavalent chromium in wastewater, *Catalysts.* 9 (2019) 1–16, <https://doi.org/10.3390/catal9120974>.
- [44] A. Serrà, Y. Zhang, B. Sepúlveda, E. Gómez, J. Nogués, J. Michler, L. Philippe, Highly reduced ecotoxicity of ZnO-based micro/nanostructures on aquatic biota: Influence of architecture, chemical composition, fixation, and photocatalytic efficiency, *Water Res.* 169 (2020), <https://doi.org/10.1016/j.watres.2019.115210>.
- [45] K.S. Ranjith, R.B. Castillo, M. Sillanpaa, R.T. Rajendra Kumar, Effective shell wall thickness of vertically aligned ZnO-ZnS core-shell nanorod arrays on visible photocatalytic and photo sensing properties, *Appl. Catal. B Environ.* 237 (2018) 128–139, <https://doi.org/10.1016/j.apcatb.2018.03.099>.
- [46] T.T. Vu, L. del Río, T. Valdés-Solís, G. Marbán, Fabrication of wire mesh-supported ZnO photocatalysts protected against photocorrosion, *Appl. Catal. B Environ.* 140–141 (2013) 189–198, <https://doi.org/10.1016/j.apcatb.2013.04.023>.
- [47] A. Torabi, V.N. Staroverov, Band gap reduction in ZnO and ZnS by creating layered ZnO/ZnS heterostructures, *J. Phys. Chem. Lett.* 6 (2015) 2075–2080, <https://doi.org/10.1021/acs.jpcclett.5b00687>.
- [48] L.V. Trandafilović, D.J. Jovanović, X. Zhang, S. Ptašniška, M.D. Dramićanin, Enhanced photocatalytic degradation of methylene blue and methyl orange by ZnO:Eu nanoparticles, *Appl. Catal. B Environ.* 203 (2017) 740–752, <https://doi.org/10.1016/j.apcatb.2016.10.063>.
- [49] N. Liu, Z. Li, Bimetal-organic frameworks derived carbon doped ZnO/Co<sub>3</sub>O<sub>4</sub> heterojunction as visible-light stabilized photocatalysts, *Mater. Sci. Semicond. Process.* 79 (2018) 24–31, <https://doi.org/10.1016/j.mssp.2018.01.004>.
- [50] M.F. Sanad, A.E. Shalan, S.M. Bazid, S.M. Abdelbasir, Pollutant degradation of different organic dyes using the photocatalytic activity of ZnO@ZnS nanocomposite materials, *J. Environ. Chem. Eng.* 6 (2018) 3981–3990, <https://doi.org/10.1016/j.jece.2018.05.035>.
- [51] S. Cho, J. Ma, Y. Kim, Y. Sun, G.K.L. Wong, J.B. Ketterson, Photoluminescence and ultraviolet lasing of polycrystalline ZnO thin films prepared by the oxidation of the metallic Zn, *Appl. Phys. Lett.* 75 (1999) 2761–2763, <https://doi.org/10.1063/1.125141>.
- [52] A.B. Djurišić, W.C.H. Choy, V.A.L. Roy, Y.H. Leung, C.Y. Kwong, K.W. Cheah, T.K.G. Rao, W.K. Chan, H.F. Lui, C. Surya, Photoluminescence and electron paramagnetic resonance of ZnO tetrapod structures, *Adv. Funct. Mater.* 14 (2004) 856–864, <https://doi.org/10.1002/adfm.200305082>.
- [53] T.M. Børseth, B.G. Svensson, A.Y. Kuznetsov, P. Klason, Q.X. Zhao, M. Willander, Identification of oxygen and zinc vacancy optical signals in ZnO, *Appl. Phys. Lett.* 89 (2006) 87–90, <https://doi.org/10.1063/1.2424641>.
- [54] M. Rabbani, M. Heidari-Golafzani, R. Rahimi, Synthesis of TCPP/ZnFe<sub>2</sub>O<sub>4</sub>@ZnO nanohollow sphere composite for degradation of methylene blue and 4-nitrophenol under visible light, *Mater. Chem. Phys.* 179 (2016) 35–41, <https://doi.org/10.1016/j.matchemphys.2016.05.005>.
- [55] M. Pirhashemi, A. Habibi-Yangjeh, Facile fabrication of novel ZnO/CoMoO<sub>4</sub> nanocomposites: Highly efficient visible-light-responsive photocatalysts in degradations of different contaminants, *J. Photochem. Photobiol. A Chem.* 363 (2018) 31–43, <https://doi.org/10.1016/j.jphotochem.2018.05.027>.
- [56] A.A. Yaqoob, N.H. Binti, M. Noor, A. Serrà, M.N.M. Ibrahim, Advances and challenges in developing efficient graphene oxide-based ZnO photocatalysts for dye photo-oxidation, *Nanomaterials* 10 (2020) 932, <https://doi.org/10.3390/nano10050932>.
- [57] G. Wang, B. Huang, Z. Li, Z. Lou, Z. Wang, Y. Dai, M.H. Whangbo, Synthesis and characterization of ZnS with controlled amount of S vacancies for photocatalytic H<sub>2</sub> production under visible light, *Sci. Rep.* 5 (2015) 1–7, <https://doi.org/10.1038/srep08544>.
- [58] T. Keijer, V. Bakker, J.C. Sloopweg, Circular chemistry to enable a circular economy, *Nat. Chem.* 11 (2019) 190–195, <https://doi.org/10.1038/s41557-019-0226-9>.